

PHY 445 (Stony Brook University): A Series of Granular Physics Experiments

Benjamin Chase & Blas Lee & Peter Koch*

(Dated: May 15, 2020)

Microscopic particles exhibit unique behaviors that are not as readily found in macroscopic systems. Electrons in an atom are arranged in orbitals and regions of probable location around a nucleus. The speed distribution for an ideal gas can be described by the Maxwell Boltzmann distribution. Under certain conditions, macroscopic particles, such as grains of sand, can exhibit behaviors generally associated with microscopic particles. We tested the conditions under which ferromagnetic steel balls exhibit microscopic behaviors using a shaking magnetic trap and high-speed camera. We found that in the presence of an external magnetic field, a system of macroscopic ferromagnetic balls can exhibit behavior that is traditionally associated with microscopic particles. The motion of these multi-ball systems was successfully modeled using the 2-D Maxwell Boltzmann distribution. We present these findings and additional results as a series of four experiments in the field of granular physics.

I. Introduction

Granular physics analyzes the collective behavior of macroscopic particles, such as grains of sand or marbles, and draws comparisons to the behavior exhibited by microscopic particles such as gases and electrons orbiting a nucleus.

In traditional experiments involving statistical mechanics, an extremely large number of particles has been necessary for the standard probabilistic measures to hold. However, in the present experiments, we were able to achieve similar results and even verify the Maxwell-Boltzmann distribution for macroscopic systems with small numbers of particles. This is accomplished by analyzing the trajectories of ferromagnetic steel balls confined by two different two-dimensional traps, which is an effective extension of Alfred Marshall Mayer's floating magnetic needle experiments in 1878 [1]. Mayer and his colleagues originally used a similar experimental set-up in order to study the atomic theory of matter and specifically the electrons in an atom. Since that original experiment, many physicists, such as Joseph John Thomson and Louis Derr, have adapted Mayer's small-scale system for their own research endeavors.

A. Previous Literature

One of the first occurrences where isolated magnets were experimented on was by Alfred Mayer in the late 1800s [1]. He first explored this phenomena to analyze the molecular model of matter, but knew that it could later have even more applications. Mayer's novel experiment consisted of needles in a basin of water. From this, he was able to observe their polarity and configurations after applying an external magnetic force. Mayer was able to analyze the configurations of different elements and compounds in a very ingenious manner and was able to create a physical illustration of when molecules solidify.

A more recent adaptation of Mayer's original experiment was performed by Bartosz Grzybowski, Howard Stone, and George Whitesides in the late 1990s [2]. The set-up consisted of small magnetic disks rotating along a liquid-air interface. The experiment was conducted to observe static and dynamic configurations and also analyze energy concentration. One discovery was that as more particles were added the system, the outermost disks displayed less homogeneous behavior and a weaker magnetic field than the innermost disks. The largest geometric formation created was a hexagonal structure of 19 disks. Conclusions detailed that this type of experiment could be significant for the discovery of new materials for engineering and multi-vortex flows.

Two other notable experiments in the field of granular physics were performed by groups at the University of Paris and University of Rostock involving Wigner crystallization [3][4]. Both studies were performed in 2D confined traps with electrons. In the study at the University of Rostock, the group concluded that phase boundaries were sensitive relative to the number of particles [3]. Observations also included 2D melting which is a significant result for our experiments as well. The study at the University of Paris found that the meta-stable states were composed of five, six, seven, nine, and nineteen steel balls, while others proved to have transitions or defects [4]. This study also provided insight regarding the N=9 dynamic configuration states, as the steel balls oriented in a (2,7) configuration under Coulombic potential but in a (1,8) lattice under a logarithmic interaction. Previous research has also shown that dense liquids exhibit behavior that obeys the Maxwell Boltzmann distribution even at low temperatures [5].

B. Equipartition Theorem

The equipartition theorem states that the energy of a system at thermal equilibrium will, on average, be evenly distributed across its degrees of freedom. Every term that appears as a quadratic in the energy equation will contribute an average energy of $\frac{1}{2}k_B T$ to the system [6]. For a system with one atom moving in the x, y, and z coordinates, its kinetic energy can be classically written as :

$$KE = \frac{1}{2}mv_x^2 + \frac{1}{2}mv_y^2 + \frac{1}{2}mv_z^2 \quad (1)$$

where each coordinate represents a degree of freedom for the atom. This even distribution of energy at thermal equilibrium is a useful tool for performing statistical analyses of granular systems.

C. Electrons

1. Orbitals and Regions of Probable Location

Electrons orbit atomic nuclei in a region of probable location that grows in radial distance as electrons gains energy and are able to overcome the attractive force from the protons inside the nuclei. These regions of probable locations can be thought of as shells that surround the nucleus.

2. Excited States

When an electron gains sufficient energy, it can move to a shell that is further away from its nucleus. This

is referred to as the excited state. The ideas of excited states and shell configurations are instrumental in granular physics because these phenomena can also be observed between macroscopic particles under certain conditions.

D. 2-D Maxwell Boltzmann Distribution

The Maxwell-Boltzmann distribution is useful for analyzing the motion of particles. Even in the case of molecular collisions the distribution still holds [8]. The term particles can refer to anything from grains of dust to coil springs, but in our case it refers to ferromagnetic steel balls. The distribution makes the following assumptions [8]:

- The diameter of the particles are smaller than the distance between them.
- Collisions between particles conserve energy.
- The particles move between collisions without interacting as a constant speed in a straight line.
- Positions and velocities are initially random.

The general form of the 2-D Maxwell Boltzmann speed distribution is [9]:

$$P(v) = \frac{mv}{k_B T} e^{\frac{-mv^2}{2k_B T}} \quad (2)$$

The most probable energy value is at the peak of the curve, when $\frac{dP}{dE} = 0$ and the average energy value is greater than the most probable energy value [8]. When temperature of the system increases, the most probable energy also increases because the distribution skews to the right, but area under the curve remains the same.

E. Magnetism

Magnetism is a useful tool to manipulate macroscopic particles to exhibit behavior originally only expected at a microscopic level. A quintessential component of electrodynamics is the physical phenomena of magnetism. On an atomic level, all magnetic materials have small currents of electrons orbiting around the nucleus along their axes [10]. In these experiments, we treated these small currents as magnetic dipoles for macroscopic systems. Under no influence, they cancel each other out due to the stochastic orientation of the atoms. However, when a magnetic field H is applied to a system, ferromagnetic materials will become magnetized and the magnetic dipoles inside them will become aligned [10].

An interesting characteristic of ferromagnetic materials, such as the steel balls utilized in this experiment, is that they retain their magnetization even after an external

field is removed. This is opposed to diamagnets and paramagnets, which magnetize parallel and opposite to the H field, respectively, but this magnetization is lost when the field is turned off.

1. Magnetic Dipoles and Interaction

Magnetic monopoles do not exist in nature, unlike electrostatic charges which can be thought of as electric monopoles. This can be proved mathematically by taking the multipole expansion of a localized current distribution [10]. A multipole expansion functions to more accurately determine the vector potential of a localized current distribution by providing an infinite sum of pole distributions that correlate with $\frac{1}{r}$. For example, the monopole term drops off at a rate of $\frac{1}{r}$, the dipole term drops off at a rate of $\frac{1}{r^2}$, and so on. The multipole expansion is an infinite series and can be expressed mathematically as follows [10]:

$$A(r) = \frac{\mu_0 I}{4\pi} \sum_0^{\infty} \frac{1}{r^{n+1}} \int r' P_n \cos(\theta) dl' \quad (3)$$

where A is the magnetic vector potential, r is the distance to the point of interest, r' is the distance to the edge of the current distribution, and θ is the angle between r and r' . P_n represents the Legendre polynomials. For any current distribution, the monopole term will always be zero because the closed loop integral around a path will always be zero. The above equation allows the derivation of the magnetic dipole moment [10] as:

$$m = I \int da \quad (4)$$

where m is the magnetic moment, I is the current and a is the area of the loop. The magnetic field of a magnetic dipole can then be defined in polar coordinates [10] as:

$$B = \frac{\mu_0 m}{4\pi r^3} (2\cos\theta \hat{r} + \sin\theta \hat{\theta}) \quad (5)$$

where m is the magnetic dipole moment and r is the distance between the point of interest and the dipole. Equation (5) indicates a $\frac{1}{r^3}$ relationship between the radial distance and the strength of the magnetic field but also a linear correlation between the magnetic dipole moment and the corresponding produced field. The key takeaway is that magnetic dipoles create a magnetic field dependent on the magnitude of their dipole moment.

2. Domains

Ferromagnetic materials do not require a continuous magnetic field to remain magnets or maintain the alignment of their dipoles over time. The catch is that the dipoles within ferromagnetic materials are

not all aligned in the same direction throughout the object [10]. The alignment is localized in groups of dipoles called domains throughout the material. When considering the material as a whole, there are many domains containing identically aligned dipoles. From domain to domain, these dipoles are not aligned in the same direction, which, over the entire material effectively cancels out the overall magnetization in the absence of an external field.

Ferromagnetic materials can be used to make permanent magnets because of their ability to maintain dipole alignment without the continued application of a magnetic field. Similar to what we will use in our experiment, consider a ferromagnetic material placed inside a large solenoid. If a current is ran through the solenoid it will generate a magnetic field within the solenoid according to the following equation:

$$B = \mu n l \quad (6)$$

where n is the number of turns in the solenoid and l is its length. The magnetic field will cause the domains within the ferromagnetic material to align, and eventually the torque produced by the magnetic field will shift the domain boundaries until every domain in the ferromagnetic material is aligned and it is magnetized [10]. This produces an induced magnetic field in the ferromagnetic material that is much more powerful than the magnetic field generated by the solenoid. This allows the use of small currents to create large magnetic fields.

When the magnetic field dissipates, the ferromagnetic material does not completely demagnetize. Since there is no torque forcing the domain boundaries to return to their original positions, it will remain a permanent magnetic until a magnetic field is applied in the opposite direction [10]. If a current moving in the opposite direction is run through the solenoid then the new magnetic field will force the domain boundaries to shift in the opposite direction as the first time, since the new magnetic field will align the dipoles in the opposite direction than they were. Now the ferromagnetic material will be magnetized but with a magnetic field pointing in the opposite direction as before. This shifting of magnetization can be represented using a hysteresis loop.

3. Hysteresis

Hysteresis is an interesting phenomenon of ferromagnetic materials which tells us that the magnetic history is significant for a particle's domains, even if there is a current external field acting on it.

A hysteresis curve shows us that the particle's magnetization is not only affected by the applied field, H ,

but also by its previous history. When a demagnetized ferromagnet has an external magnetic field applied to it, the parallel magnetization increases to a certain point as the domains align with the field's direction [10]. Disabling the external field will not completely demagnetize the particle due to the interaction of the spins. If the external field is increased in the same direction, the magnetization will saturate.

When domains inside of a material change directions, this causes energy to dissipate because of internal friction between the domains [10]. It is important to note that in ferromagnetism, dipoles within certain domains align parallel to each other. Dipoles cannot be significantly misaligned even with random thermal motions, unless the temperature of the system is very high.

The specific temperature at which certain materials lose their permanent magnetic properties is called the Curie temperature. It is comparable to the boiling point or freezing point of a liquid in that it does not induce a gradual transition from ferromagnetic to para-magnetic behavior. These abrupt changes in a material can be referred to as phase transitions.

4. Dipole-Dipole Interaction

An external magnetic field can cause ferromagnetic material to form magnetic dipoles when their domains are forced to shift. These dipoles exert a magnetic field as in equation (5), which means that magnetic dipoles can either attract or repel one another. Two ferromagnetic materials inside an external field can either attract or repel one another depending on the alignment of their domains. A cluster of ferromagnetic balls subject to the same magnetic field will repulse each other at all times, as will be seen in our experiments.

5. Influence of Quantum Spin and Torque

One fundamental property associated with magnetic dipoles is the quantum spin of the electron [9]. The Pauli Exclusion Principle states that two electrons in the same orbital must possess different spins. When all states are completely filled, the atom has no net spin, meaning the only magnetic contributions are those that arise from orbital motion.

Magnetic dipoles also experience torque from H , similar to how an electric dipole does in an electric field. When two magnets are brought within close proximity of each other, one will rotate to align itself with the other. In this case, the external field H creates a magnetic torque on the magnets forcing them to rotate. For these experiments, the ferromagnetic spheres would not experience this when motionless, because the magnetization is parallel to the external field. However, when

human manipulation enables them to roll, their orientations change and a restoring torque is produced. Mathematically, torque on a small magnet can be calculated as:

$$\tau = m \times B = \mu_0 m \times H \quad (7)$$

where m is the magnetic moment, B is the magnetic field, μ_0 is the vacuum permeability constant, and H is the external magnetic field.

F. The Present Experiments

We test the individual and group behavior of ferromagnetic steel balls through several experiments that utilize an external magnetic field generated by a solenoid.

In the first experiment we use a concave lens and a small ferromagnetic ball to calculate an experimental value of the acceleration due to gravity. This will be achieved by allowing the ball to freely oscillate across the concave lens as its motion is recorded by a high-speed camera.

In the second experiment we build upon the first by analyzing the oscillatory motion of the ball in the presence of both AC and DC magnetic fields. We will develop a predictive model for damping coefficients and natural frequency as a function of both AC and DC currents.

In the third experiment we analyze the lattice formations of multiple steel balls on a flat surface subject to an external AC magnetic field. We also observe 2-D melting behaviors for various currents and number of balls.

In the fourth experiment we build upon the third by comparing the velocity distribution of multiple ferromagnetic balls to the 2-D Maxwell Boltzmann distribution.

II. Tracking Software

All four of our experiments strongly relied on the use of tracking software to collect data.

A. ImageJ

ImageJ [12][18] is a Java-based software that can perform standard image processing and has many plugins that offer analytical uses to researchers in biology, physics, and chemistry. We used the Mosaic plug-in that offers 2D particle tracking functionality. This is largely useful for cell biologists and has direct application to granular physics experiments. We tracked the

coordinate motion of our ferromagnetic balls for all four experiments.

B. Alternative

Due to persistent technical difficulties, we attempted to use MATLAB [16][17] to program our own version of the 2D particle tracker offered by ImageJ. This would have made analyzing data from our experiment significantly easier and less arduous. We present our findings and algorithms for programming a particle tracker in the hopes that this information will further future granular physics experiments.

C. Tracking Algorithm

1. Image Processing Toolbox

A key feature of MATLAB that allows for particle tracking is the image processing toolbox [11]. This toolbox includes a built-in function that detects circles in an image and returns their coordinates. This function is crucial because the videos from the camera can be processed as individual frames which are essentially a collection of images. This built-in function can then be used to find the ferromagnetic balls in each frame because they are simply circles when looking down along the z-axis.

2. Circle-finding Algorithm

a. Centers The image processing toolbox uses a Circular Hough Transform based algorithm to identify and define circles in different images [13]. An essential feature of this algorithm is identifying candidate pixels that might represent the center of a circle based on their brightness and contrast gradient. These candidates then 'vote' for pixels such that these pixels form a circle around the candidate pixel [13]. When all of the candidate and vote pixel are stored in an array, the true centers of circles in the image are determined by looking for peaks in the array.

b. Radii The radii often have to be computed as a separate step in the algorithm [13]. Radii are determined by several inputs that the built-in function can accept. These include sensitivity, edge threshold, and minimum and maximum radius values. Depending on the values provided, the algorithm will use the peak data from the center pixel array in conjunction with the brightness and contrast gradient values of the image to determine the radius of each circle.

3. Single Particle

For a single particle, the programming for the tracking software is rather simple using the image processing toolbox. After brightness and contrast and input values are properly adjusted, each frame of the video is iterated over. During each iteration, the built-in function detects the circle and its center and radii information is stored in respective arrays. After all of the iterations are complete, the center coordinates of each frame are sent to a csv file, from which they can be analyzed and plotted to examine the motion of the particle. The radii data is used to check for accuracy across frames.

4. Multiple Particles

The programming for multiple particles is identical as for single particles, but requires additional steps. The built-in functionality of the image processing toolbox processes each frame of the video independently. This means that in each frame, the circles are detected in an unpredictable order. For the single particle case this is not a problem, but as N increases past 1, this becomes a fundamental obstacle to properly tracking each particle's coordinates throughout the video.

We solved this problem by linking particles from one frame to the next. In the first frame, the center coordinates of each particle are stored in individual arrays in a cell. In the second frame, the program iterates over each particle and compares its distance to each of the center coordinates in the previous frame. The coordinates of each particle in the current frame are then added to the array that holds the closest particle in the previous frame. Since each frame is roughly 1/210 seconds, this method will never link the wrong particles to one another.

5. Brightness and Contrast

The image processing toolbox utilizes the brightness and contrast gradients to identify areas of the image that constitute a circle [13]. To ensure that this process goes smoothly, it is necessary to invert the colors of the frame and adjust the brightness and contrast of each frame before processing for circles. This is done by adjusting the brightness and contrast of each frame to a scale that magnifies the contrast between the background and particles.

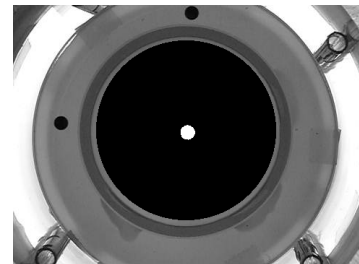


FIG. 1. Adjusting the brightness and contrast to better identify circular particles.

6. Radius and Edge Blur

The image processing toolbox can accept minimum and maximum radius pixel values. Setting these closer together ensures that only particles around the size you are looking for are found, and considerably speeds up the circle-finding algorithm.

Even at roughly 210 frames per second, the ferromagnetic balls can move sufficiently fast to cause blurring on the ball's edge when viewed frame by frame. This can make it difficult for the image processing toolbox to properly identify the ball. To correct for this, the input values for edge threshold and sensitivity must be raised or lowered to allow the algorithm to identify imperfect circles.

7. Accuracy

To quantitatively make sure the program properly tracks the particles, we compute the standard deviation of the radius for each particle throughout each video. We generally expect this standard deviation to be within 2% of the average radius for precision. The program will also return an error if more than the specified number of particles is found in any frame, meaning that it cannot return coordinates unless it is successful. This might be seen as either a limitation or as a positive feature.

8. Preview

We created a preview feature that allows us to test our input values before committing to tracking the entire video. As a preview, the program uses the input values to track 1/20 of the frames evenly spaced out. This allows us to confirm that our inputs will work properly for the entire video.

D. Comparison to ImageJ

Unfortunately the alternative program developed in MATLAB is not precise enough to use for analysis in these experiments. As shown in the following section, the center coordinates between programs are very similar and are generally sufficient to use as a trajectory mapping tool. Despite this, the lower precision of the MATLAB software causes significant miscalculations of the velocity values. The coordinates created by ImageJ are precise to the thousandths place, while the image processing toolbox in MATLAB only provides coordinates that are precise to the hundredths place, and sometimes even the tenths place.

1. Procedure

It is uncertain what algorithm ImageJ uses to track particles. ImageJ provides a user-friendly GUI that hides all of the programming and makes it easy to use.

The radius value allows the user to specify one radius that the program uses throughout the tracking process [12]. This is faster and more efficient than specifying a minimum and maximum radius as in the MATLAB program. Unfortunately the image processing toolbox does not function properly without a generous radius range. For our tracking in ImageJ, we found that a radius between 9 and 13 worked best.

The cutoff value allows users to specify a score that the program uses to dismiss possible particles as invalid [12]. This can help clean up noise during tracking, but in our experience we found that the cutoff often causes legitimate particles to be dismissed along with the noise. As such, we always set the cutoff to 0.

The percentage value allows users to specify which percentile of the brightness gradient the program will use to search for particles [12]. We always set the percentage value to 1.

2. Coordinates

We compared the center coordinates output by ImageJ with those generated by our MATLAB program for an identical video.

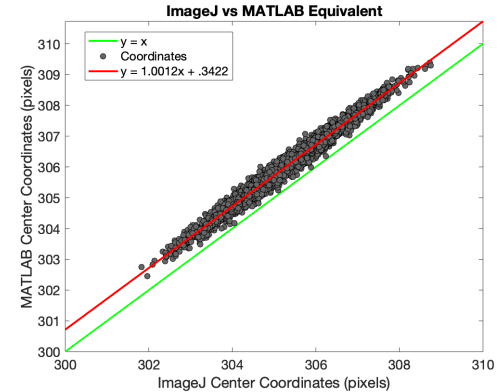


FIG. 2. Center coordinate comparison between ImageJ and our program designed in MATLAB. The average difference between coordinates in each frame is .7227 pixels (SD = .1473).

The average difference between the center coordinates for each program is significantly different from 0 ($p < .01$). This level of precision was not enough to suffice when performing further data analysis.

3. Velocities

The same comparison can be done for the velocities calculated between programs, with which the disparity between the two programs becomes more apparent.

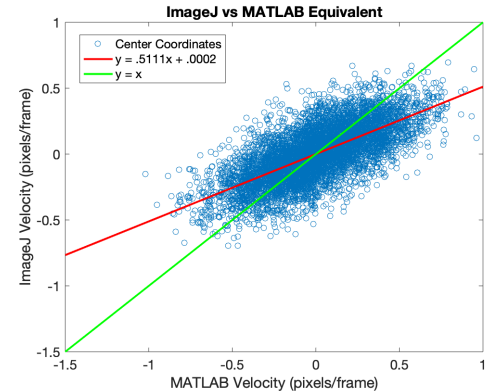


FIG. 3. Velocity comparison between ImageJ and our program designed in MATLAB. The average difference between velocities for two frames is .0000386 pixels per second (SD = .2066).

The average difference between velocities is not significantly different from 0 ($p = .9881$). The trend line shows that the velocity data is significantly worse than the center coordinates data. The maximum velocity value calculated by ImageJ is .6962 pixels/second, while our program finds a maximum velocity of .9621 pixels/second. Our program finds a minimum velocity of -1.0204 pixels/second while ImageJ finds a minimum of

- .6961 pixels/second. It is apparent that the lower precision of our program's coordinates leads to significant over-measuring of the velocity values.

III. Error

All of the laboratory measurements in this study were measured using imaging software and eventually propagated through various functions and additional software. To avoid excessively meticulous propagation of error that would require many assumptions, we instead relied on repeated trials and the error given for fitting parameters to properly account for uncertainty throughout our experiments.

1. Random Error

Random error is best considered as an uncertainty due to small variations between trials. It can also be a result of instrumental limitations. Random error can be reduced by taking a significant number of trials since as the number of N trials approaches a large number, the average value will approach the true value of the measurement. This technique can also be used to significantly reduce random error only using a small number of trials, as we did in our experiments. The error on our fitted parameters is taken from a 95% confidence interval for the fitted parameter.

2. Systematic Error

Systematic error is best considered as error resulting from a mistake or calibration problem. For example, using a ruler to measure a length but starting to count from one inch instead of zero inches. This error cannot be reduced through multiple trials. Possible systematic error in our experiment is human error as well as imperfections in the apparatus.

IV. Experiment 1

In experiment 1, we calculate an experimental value of the acceleration due to gravity using a small steel ball and a concave lens.

A. Methods

All data analysis and plotting was done using MATLAB [7].

1. Equipment

In the first two experiments, the Gravito-Magnetic (GM) trap is utilized. It incorporates a concave lens and ferromagnetic steel balls that are primarily influenced by gravity, which allows for the analysis of their oscillations. The GM trap also has a solenoid that can produce a magnetic field in its system. We will not be using a magnetic field in this experiment but it is a fundamental piece of the GM trap. The uniformly magnetized steel spheres in this experiment had a diameter of 3.5mm and the concave lens had a radius of 38.6 mm.

Since data collection is taken in accordance with a 2D plane, a plexiglass leveling component is also used. Plexiglass, a common thermoplastic, is preferred due to its high tensile strength and resistance to plastic deformation. This is necessary because if the planar level ever needs to be adjusted, the plexiglass can be adjusted using a wedge. Although it has a high tensile strength, a noticeable drawback to this choice in material were minor stress cracks that, if persistent, could cause the trap to fall.

For data collection, a Casio high speed camera was used for recording the paths of the particles. Movement was recorded at 209.78fps with an image plane of 480 by 360 pixels. This camera was mounted on steel bars above the trap with a vertical downward view of the lens. The bars had adjustable knobs in the case that the camera was not properly leveled. This was important to ensure a proper angle and also to make sure the capture angle was symmetric relative to the 2D coordinate system of the trap. If the plane was slightly off, our tracking coordinates would be flawed.

2. Procedure

After setting up the camera and using manual focus with the GM trap in the frame, we used a microscope to select a ferromagnetic ball without visible impurities. Then we cleaned the chosen ball with an acetone solution. We released the ball from the radial edge of the concave lens. It was important that the trajectory of the release was vertically aligned with the plexiglass plane, such that the ball oscillated in only one direction. After performing multiple launches for one recorded video, the best launches were selected later for tracking and analysis. When the video recording was completed, the SD card was removed from the camera and used to load the files into the laboratory computer. After trimming the best launches with KMPlayer, ImageJ was utilized to track the trajectory of the ball.

3. Conversion Factors

To analyze our data it is necessary to determine the conversion factor between the pixels in the video and meters. We determined the conversion factor by measuring the distance across the concave lens using a ruler and comparing it to the same distance given in pixels. We found this conversion factor to be:

$$p = .000194 \pm .000003m \quad (8)$$

4. Kinematics

Barring imperfections in the ball or the lens' surface, the ball should undergo damped simple harmonic motion that will decay due to friction between the ball and the lens. Consider the following diagram to illustrate this setup:

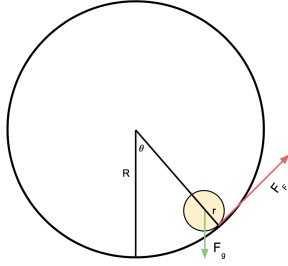


FIG. 4. Ball of radius r oscillating along the concave lens. Created in Google Drawings.

Using the moment of inertia for a solid sphere to be $\frac{2}{5}mR^2$, the differential equation describing the motion of the ball rolling on the concave can be found [9]:

$$\ddot{\theta} = -\frac{5g}{7(R-r)} \sin(\theta) \quad (9)$$

where θ is the angle between the ball and the z axis, R is the radius of the concave lens, and r is the radius of the ball. The motion of the ball on the concave lens is analogous to the motion of a pendulum exhibiting simple harmonic motion. The $R - r$ term serves to align the center of mass of the sphere with θ since the actual motion would trace out a pendulum with length $R - r$ because the center of the sphere will always be a distance r from the surface of the lens. The equation of motion can be used to find the natural frequency of the ball, analogous to a pendulum [9]:

$$\omega_0 = \sqrt{\frac{5g}{7(R-r)}} \quad (10)$$

where ω_0 is the natural angular frequency. Since R and r will be known, we can experimentally calculate g by measuring the period of the ball as it oscillates across

the lens.

Since there is a non-zero friction force between the ball and the surface of the lens, and in practice between the ball and the air as well, a damping coefficient must be incorporated into our model for the motion of the ball. The equation for motion can be written as [9]:

$$\theta(t) = Ae^{\beta t} \cos(\omega t + \phi) \quad (11)$$

where A is the amplitude of the motion, β is the damping coefficient, and ω is the angular frequency. Equation (12) provides the relationship between the angular frequency of the motion and natural angular frequency:

$$\omega = \sqrt{\omega_0^2 - \beta^2} \quad (12)$$

5. 2-D Analog

The high-speed camera will not be able to capture the height of the ball as it oscillates along the surface of the lens. We will only be able to record x and y data that corresponds to the ball's position on the surface of the lens as if it was flat not concave.

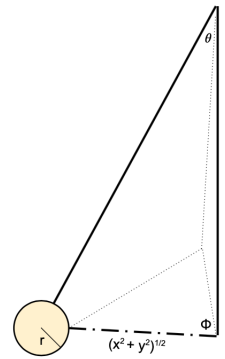


FIG. 5. 2-D analog of oscillations as seen by the camera to derive θ . Created in Google Drawings.

Using the radius of the lens and the ball, we can use express the angle between the axes of the sphere and the ball in terms of its x and y coordinates and the radii values. Since R points along the z-axis, which is always perpendicular to the plane of the lens as seen by the camera, the angle ϕ will always be a right angle. The angle that the ball makes with the z-axis is given by:

$$\theta = \tan^{-1}\left(\frac{x^2 + y^2}{R - r}\right) \quad (13)$$

where θ is the angle between the ball and the z axis, and x and y are are coordinates of the ball as seen by the camera looking down along the z-axis. We will be calculating ω and θ from our experimental data of the motion of the ball and using it to fit equation (11) and solving for A , β , ω , and ϕ , which will allow us to solve for ω_0 in equation (12) and finally for g in equation (10).

B. Results

We successfully fit the motion of our ball to equation (11) and calculated an experiment value for the acceleration due to gravity.

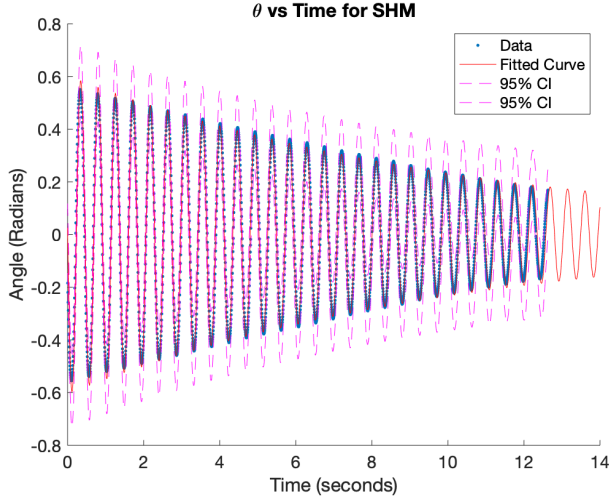


FIG. 6. θ vs time using equation (11) for oscillations on concave lens. $\chi^2(2652) = 96.524$, $p = 1$

TABLE I. Fit Parameters for $\theta(t)$

Parameter	Fitted Value
A (rad)	0.6053 (0.5993, 0.6113)
$\beta (s^{-1})$	0.09490 (0.09297, 0.09684)
ϕ (rad)	1.528 (1.519, 1.538)
ω (rad/s)	13.74 (13.74, 13.74)

We found that the acceleration due to gravity is $9.74 \pm .02 \frac{m}{s^2}$. Using $9.81 \frac{m}{s^2}$ as the accepted value of the acceleration due to gravity, we find that our experimental results are significantly different from the expected value ($t(3) = 3.5$, $p < .01$).

C. Discussion

The function given by equation (11) fit the motion of the ball extremely well. This resulted in relatively precise values for our fitted parameters. Our experimental value of g derived from the fit using equations (10) and (12) had a small relative error due to the extremely successful fitting averaged over multiple trials. Statistically our result is significantly different than the accepted value, however, we can make the qualitative observation that our result for g is relatively close to the accepted value. We also found a very precise value for the angular frequency of the ball from our fit, shown in table I.

V. Experiment 2

In experiment 2 we repeat the single ball launches from experiment 1 under the influence of an external AC and DC magnetic field. We determine experimental relationships between current applied through a solenoid and damping coefficients as well as natural angular frequency for both cases.

A. Methods

1. Equipment

Unless otherwise stated, the same apparatus and materials from the first experiment were used with the following additions.

Variable current was supplied to the solenoid via the standard Variac or DC power source. The Gravito-Magnetic trap also includes a multi-meter for measuring the current that runs through the solenoid to produce the magnetic field within the targeted area inside the trap. It is noteworthy that AC currents did not exceed 0.6A for a prolonged period of time to avoid the solenoid from overheating.

The trap also included electronic equipment that played a key role in general functionality. A crucial component within the setup is the adjustable capacitor which allows the system to stay in natural resonance since it is an effective RLC series circuit. Theoretically, resonance occurs since energy is stored in both electric and magnetic fields. This is a necessary phenomenon in order to minimize vibrations and noise. For this experiment, the resonant frequency was held close to 60Hz.

2. Procedure

Barring the following additions, the procedure is identical to experiment 1. While the camera is recording, we varied the AC Variac up to 1.2 Amperes. The ferromagnetic ball should oscillate back and forth inside the trap and could have a different count of oscillations per trial. Once again, the videos were trimmed to isolate the best launches with the KMPlayer and Image was used to track the trajectories. We repeated the same procedure for DC current up to .6 Amperes using a DC power source.

3. Kinematics in a Magnetic Field

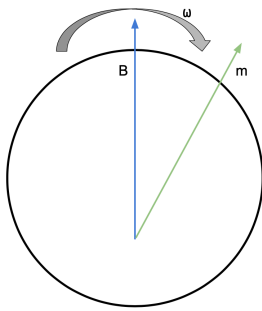


FIG. 7. [Influence of an external magnetic field on a ferromagnetic ball oscillating along the concave lens. Created in Google Drawings.

Since the ball is ferromagnetic, the external magnetic field will produce a torque and align all of the dipoles in the same direction throughout the ball, inducing a magnetization. When the ball rolls, the magnetization vector, which represents the alignment of the domains, will rotate away from the magnetic field. When this happens, the magnetic field will exert a torque to maintain the alignment of the domains. This creates an internal friction that opposes the angular motion of the ball and provides an additional source of damping. The torque produced by the magnetic field is given by [9]:

$$\tau = -mB\sin(\phi) \quad (14)$$

where ϕ is the angle between the magnetization vector and the magnetic field. In the case of a DC magnetic field, the direction of the magnetic field will not change throughout the ball's motion. At all times, the torque produced by the magnetic field will directly oppose the motion of the ball, providing constant additional damping. In the case of an AC magnetic field, however, the direction of the field changes periodically. When the magnetic field vector points upwards it will oppose the angular motion of the ball, and when it points downwards it will drive the angular motion of the ball.

In the case of an AC magnetic field, the damping coefficient and natural angular frequency values must be adjusted due to the torque exerted by the external magnetic field [9]:

$$\beta' = \frac{\beta + cI^\alpha}{1 + aI^\alpha} \quad (15)$$

$$\omega'_0 = \frac{\omega_0}{\sqrt{1 + aI^\alpha}} \quad (16)$$

where I is the current driven through the solenoid and a , α and c are fitted parameters. We determine the function for the adjusted damping coefficient and natural angular frequency in the case of a DC magnetic field

experimentally. Since the DC magnetic field will always oppose the motion of the ball, we expect the damping to be significantly greater than in the case of the AC field.

B. Results

1. Damping

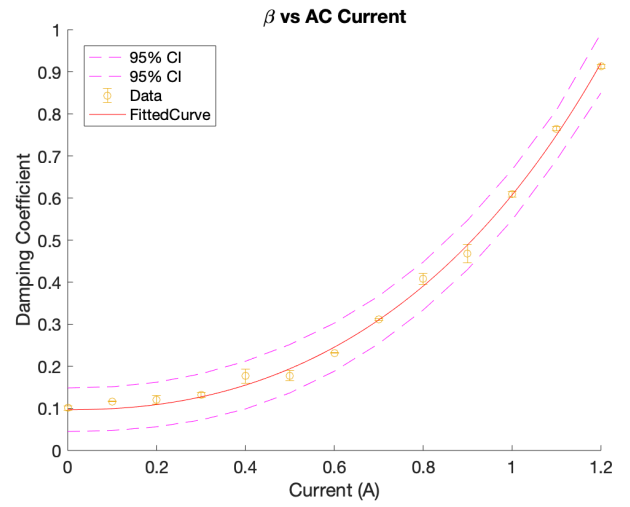


FIG. 8. Fit of damping values against AC current using equation (15). $\chi^2(12) = 2.57$, $p = .998$.

TABLE II. Fit Parameters for AC $\beta'(I)$

Parameter	Fitted Value
a	-0.3457, 0.1121
c	0.2877, 0.5908
α	2.246, 1.714, 2.777

To best fit our damping coefficients with DC current, we introduced a multiplicative constant into equation (15) such that:

$$\beta' = z \frac{\beta + cI^\alpha}{1 + aI^\alpha} \quad (17)$$

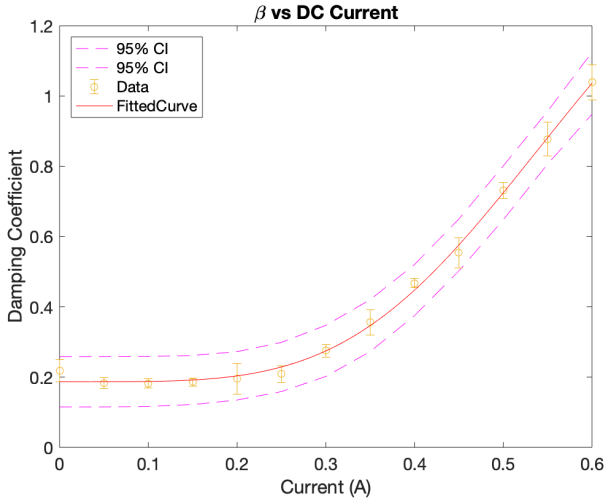


FIG. 9. Fit of damping values against DC current using equation (17). $\chi^2(12) = .102$, $p = 1$.

TABLE III. Fit Parameters for DC $\beta'(I)$

Parameter	Fitted Value
a	8.167 (-3.519, 19.85)
c	18.26 (1.057, 35.46)
α	4.176 (3.173, 5.179)
z	.8565 (.7718, .9413)

2. Natural Angular Frequency

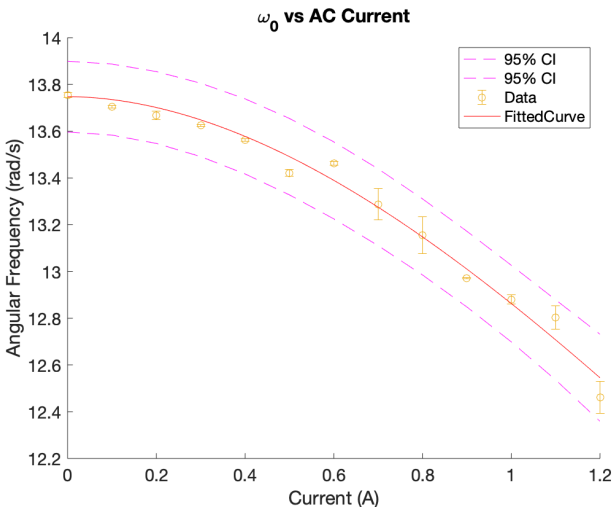


FIG. 10. Fit of natural angular frequency against AC current using equation (16). $\chi^2(12) = 2.595$, $p = .998$.

TABLE IV. Fit Parameters for AC $\omega'_0(I)$

Parameter	Fitted Value
a	.1424 (.1337, .151)
α	1.89 (1.622, 2.158)

In contrast to the damping coefficient fit for DC current, we did not introduce an additional constant to make the DC current fit for natural angular frequency.

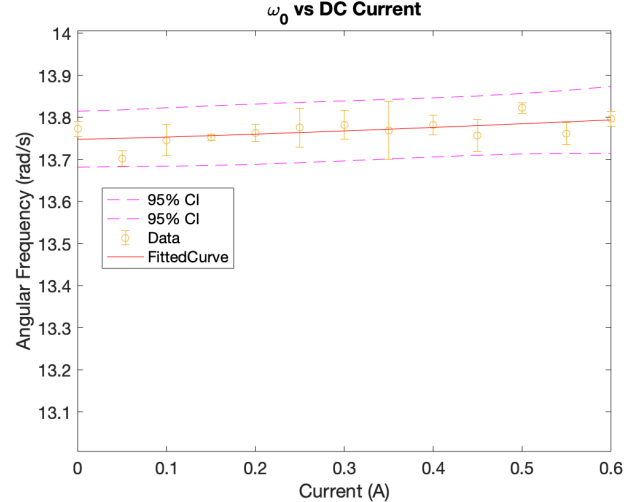


FIG. 11. Fit of natural angular frequency against DC current using equation (16). $\chi^2(12) = .325$, $p = 1$.

TABLE V. Fit Parameters for DC $\omega'_0(I)$

Parameter	Fitted Value
a	-.01235 (-.03178, .007077)
α	1.211 (-.7165, 3.138)

C. Discussion

All four of our fits were extremely successful. Beyond the χ^2 and p values, we can see that all of our data points and their error bars fell within the 95% confidence intervals given for each fit.

In both cases, the external magnetic field had an exponentially positive effect on the damping coefficient. We can qualitatively observe that the DC current had a significantly greater contribution to the damping than the AC current. The damping coefficient measured for a DC current of .6 A is similar to the damping coefficient measured for an AC current of 1.2 A. This supports our analysis that the DC current is constantly opposing the angular motion of the ball while the AC current drives it some of the time.

It is worth noting that between figures (12) and (13) we observe a significantly different starting point for the damping coefficient when the current is set to 0 A. This is likely a result of performing the DC trials shortly after the ball was exposed to an external magnetic field. We could have corrected for this by using a new ball.

Based on equations (15) and (16), we expect that the fitted values of a and α would agree between the AC current fits for the damping coefficient and natural angular frequency. We find that neither the α values nor the a values are significantly different within 3 standard deviations. We also note that the confidence interval for the a value given by table II is significantly large with respect to the actual value.

It is worth noting that the confidence intervals for some of our fitted parameters are significantly large with respect to the parameter value, notably for table III.

In an AC magnetic field, we can observe that the current had a significant negative effect on natural angular frequency. In the DC magnetic field, however, we can see qualitatively that the current did not have a significant effect on the natural angular frequency. The maximum amplitude of the confidence interval in figure 14 is roughly .15 radians. The relationship between DC current and natural angular frequency would likely be better modeled as a linear fit instead of by equation (16). The standard deviation of the natural angular frequency values for AC current is .402 radians, compared to .028 radians for DC current.

The natural angular frequency behavior between AC and DC current might be explained by the interaction between each magnetic field and the ball. Since the DC magnetic field is always opposing the ball's motion, the force on the ball is not fluctuating as the magnetic field flips directions every half-cycle. In the case of the AC field, the ball's motion is sometimes driven and sometimes opposed, which can decrease the angular frequency as the current increases. This is not possible with a DC magnetic field.

VI. Experiment 3

In the third experiment we analyze the lattice formations and melting behavior of systems with multiple ferromagnetic steel balls.

A. Methods

1. Messenger Ball

The messenger ball serves to provide a benchmark for calibration to ensure the system does not have signifi-

cant extraneous motion and that the ferromagnetic balls are significantly moving over time with respect to the platform at high currents. The overall motion of a messenger ball and a ferromagnetic ball at a relatively high current can be analyzed to confirm that, even at high currents, the magnetic forces between the ferromagnetic balls drive motion separate from the platform's motion.

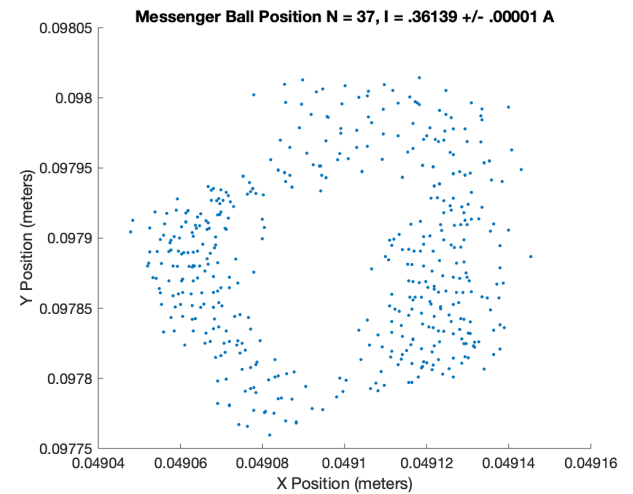


FIG. 12. Coordinates of a ceramic messenger ball plotted over time.

The maximum amplitude of the messenger ball is .00012 (.00001) meters.

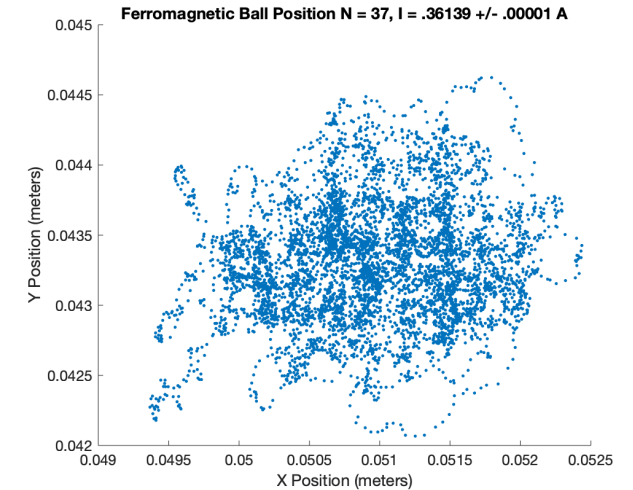


FIG. 13. Coordinates of a ferromagnetic ball plotted over time.

The maximum amplitude of the ferromagnetic ball is .0015 (.0001) meters. These results are significantly different ($p < .01$) by roughly a factor of 10. This measurement is only shown for one trial, but illustrates that we are able to confirm the overall motion of our ferromagnetic balls is due to their magnetic interactions not extraneous movement of the platform.

2. Shaker

The shaker constantly injects energy into the system to simulate randomness. Despite the constant shaking of the surface on which the balls will be rolling, the repulsive forces created by their induced magnetic fields will prevent collision at sufficient currents and simulate an ideal gas. We set the shaker to a constant digital frequency of .0993 kHz. Since the shaker is composed of 5 individual fan blades, we have to divide this frequency by 5 to obtain the true frequency of the shaker with respect to the platform: .01986 kHz.

Although the overall amplitude of the messenger balls is significantly lower than that of the ferromagnetic balls, the amplitude at specified frequencies should not be. As long as the platform is oscillating via the shaker, the ferromagnetic balls on the platform will oscillate back and forth as well - but with a lower amplitude. Using the moment of inertia of a solid sphere to be $I = \frac{2}{5}mR^2$, the ratio between the amplitude of the platform and ferromagnetic ball can be found [9]:

$$\frac{A_P}{A_B} = \frac{7}{2} \quad (18)$$

This amplitude ratio should hold true for motion at the shaking frequency of .01993 Hz.

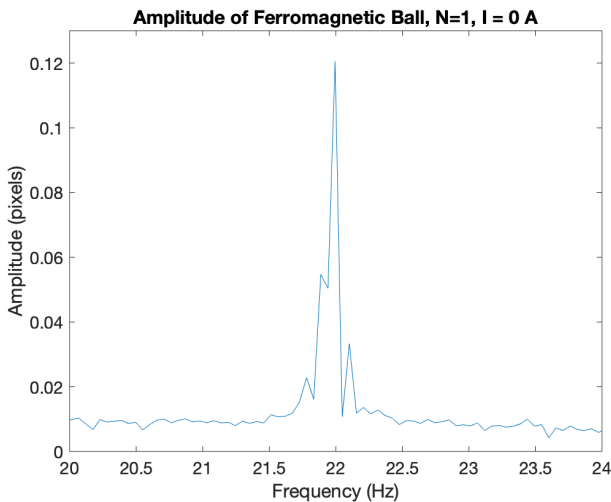


FIG. 14. Fourier transform to show ferromagnetic ball amplitude for single ball oscillation at current = 0 A. Created using [14].

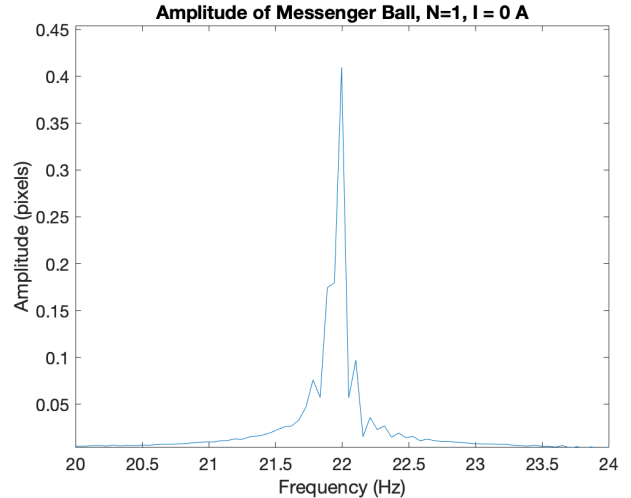


FIG. 15. Fourier transform to show messenger ball amplitude for single ball oscillation at current = 0 A. Created using [14].

We find that, for one trial, the amplitude ratio is 3.39 (.02). Although this result is only taken from one trial and is significantly different from the expected value of 3.5 ($t = 5.5$), we can qualitatively observe that our result is reasonably close to the theoretical value. It is also worth noting that the amplitude peaks at 21.99 (.01) Hz which is significantly different than the expected 19.86 Hz ($t = 213$). Perhaps the apparatus had systemic imperfections such as being too loose or too tight, which interfered with the platform oscillating at the shaker's frequency. It is also possible that there were imperfections on the ball for this trial, causing it to not oscillate as a perfect sphere.

We expect that the magnetic interactions between the ferromagnetic balls in the presence of an AC magnetic field will force them to form 2-D lattices at high currents and exhibit melting behavior as the current decreases.

3. Equipment

We utilized the All-Magnetic (AM) trap instead of the GM trap. The primary difference between these two traps is in the restoring force that keeps the magnetic spheres confined within the frame for analysis. Instead of a concave lens, the AM trap utilizes a flat surface and a ferromagnetic ring that repels spheres from the border. In conjunction with the energy injected into the system by the shaker, the AM trap allows for measurements of dynamic motion. Aside from electronics, the system also incorporates a support structure and a "shaker". The purpose of the shaker is to inject energy and create a dynamic, randomized environment for the balls. The AM trap makes it possible to analyze the effects of magnetism and shaking on dynamics, leading the system to emulate a heat bath. It is also noteworthy

that an air puffer was introduced in order to create randomness and reset the configurations in between trials.

4. Procedure

Moving over to the AM trap, we prepared the camera for video collection in a similar manner as before. We gathered sets of 9, 19, and 37. For the case of $N = 9$, we observed the differing 1-8 and 2-7 configurations upon arousal. We recorded four sets of 25 trials using a varying AC current up until 0.6 Amperes. It is important not to exceed 0.6A with the AM trap to prevent the solenoid from overheating. It is also important not to touch the system in general because the phasor voltages over the LC circuit are quite large and can be dangerous. For each trial, we turned on the current and frequently perturbed the system using the air puff. We repeated this 25 times for each current value.

For the analysis of 2D melting, we removed any existing balls in the system and activated the shaking trough to let it settle over time. We took a 30 minute pause before collecting data to allow the shaker to settle. We varied the AC current for $N = 9, 19$, and 37 balls to observe when the system loses order and exhibits melting behavior. As the current decreased, we expected the order within shells to become more chaotic. This is what we refer to as melting. Some systems have multiple stable states, so we made sure to take note of transitions that occur between shells. Lastly, due to technical problems with ImageJ, we utilized the MATLAB algorithm to produce the trajectory diagrams for this experiment. Since we are not performing data analysis with coordinates, the program should suffice for simply producing trajectories.

B. Results

1. Orientations

We first observed the lattice formations for each system at a high current that kept the balls extremely stable.

2. $N = 9$

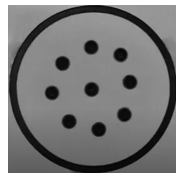


FIG. 16. An Example of the 9 Ball Lattice Formation. We refer to this as the 1-8 configuration.

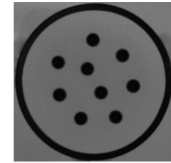


FIG. 17. An Example of the 9 Ball Lattice Formation. We refer to this as the 2-7 configuration.

3. $N = 19$

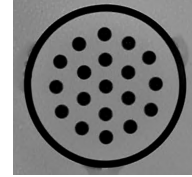


FIG. 18. An Example of the 19 Ball Lattice Formation. We refer to this as the 1-6-12 configuration.

4. $N = 37$

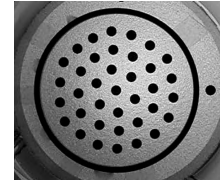


FIG. 19. An Example of the 37 Ball Lattice Formation. We refer to this as the 1-6-12-18 configuration.

5. Probability of States

We test the stability of different lattice configurations for systems with $N > 3$ balls. There can be more than one configuration that these systems find themselves in equilibrium. For example, the $N = 9$ system might achieve an inner ring of 1 ball and an outer ring of 8 balls in one equilibrium state, or an inner ring of 2 balls and an outer ring of 7 balls in another equilibrium state. These two different configurations might have different levels of stability, i.e. one configuration might be more probable to find in nature if many systems are left to achieve their own equilibrium over time.

To test which configuration of the $N = 9$ ball system is more stable, we added energy into the system using the shaker at a frequency of .0993 Hz. Then we varied increments of AC current through the solenoid to induce magnetic fields inside each ball and allowed repelling forces between magnetic dipoles and the outside ring to force the balls into one of two equilibrium states. After allowing roughly 10 seconds to observe any changes in the equilibrium configuration,

we turned off the current and repeated the test. We repeated this for 25 trials under three different currents.

TABLE VI. Probabilities of different equilibrium configurations of the $N = 9$ system over 25 trials at each current.

Current [A]	Trials	Probability of 1-8	Probability of 2-7
0.141 ± 0.001	N/A	too chaotic	too chaotic
0.163 ± 0.003	N/A	too chaotic	too chaotic
0.320 ± 0.003	25	88%	12%
0.503 ± 0.003	25	80%	20%
0.669 ± 0.003	25	60%	40%

For the first two currents measured, the lattice formations were not stable enough to provide meaningful data.

An interesting phenomena noticed during data collection was that there were multiple different types of 2-7 configurations. In addition to the straight orientation shown in Figure 21, we also observed the skewed orientation displayed below.

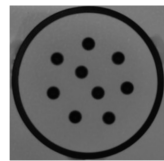


FIG. 20. An Example of the 2-7 Skewed Orientation.

The final 2-7 orientation that we noticed is referred to as the rotated orientation. In this equilibrium, the balls in the inner shell are rotated with respect to the balls seen in the other two patterns.

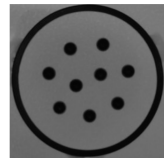


FIG. 21. An Example of the 2-7 Rotated Orientation.

It would have been ideal to repeat this test for varying currents across more than three numbers of balls, but perhaps that idea can be tabled for future experiments.

6. Melting

We analyzed orbital melting by identifying the current at which balls in an orbital shell transitioned into another shell by swapping with a ball in another shell. This current might be referred to as the threshold current at which the interactions between the magnetic

dipoles are no longer strong enough to maintain the lattice formation. We tested this threshold current for 9, 19 and 37 balls.

7. $N = 9$

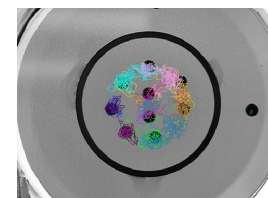


FIG. 22. Overall 2D Melting for 9 Particles at $I = .25 (.01)$ A.

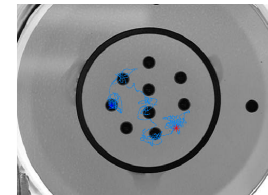


FIG. 23. First Example of Shell Transitions for $N = 9$, $I = .25 (.01)$ A.

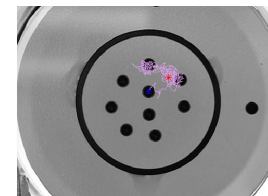


FIG. 24. Second Example of Shell Transitions for $N = 9$, $I = .25 (.01)$ A.

8. $N = 19$



FIG. 25. Overall 2D Melting for 19 Particles, $I = .154 (.001)$ A.

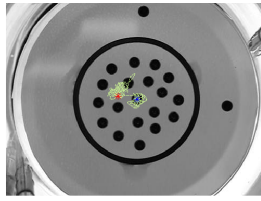


FIG. 26. First Example of Shell Transitions for $N = 19$, $I = .154 (.001)$ A.

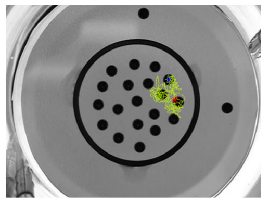


FIG. 27. Second Example of Shell Transitions, $N = 9$, $I = .154 (.001)$ A.

9. $N = 37$

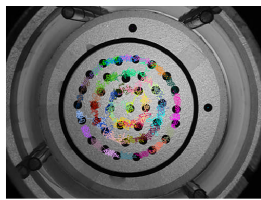


FIG. 28. Overall 2D Melting for 37 Particles, $I = .20189 (.00001)$ A.

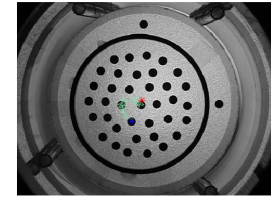


FIG. 29. First Example of Shell Transitions, $N = 37$, $I = .20189 (.00001)$ A.

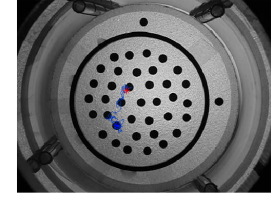


FIG. 30. Second Example of Shell Transitions, $N = 37$, $I = .00001$ A.

C. Discussion

We found the 1-8 configuration to be more stable than the 2-7 configuration over the 75 trials. This might be analogous to electrons in individual atoms and explained by a 'full' outer shell serving as a more stable equilibrium configuration than a partially filled outer shell. However, as the current was increased for the system which increased the magnetization of each ball and the magnetic forces between them, the probability of the 2-7 configuration increased. At higher currents, the larger magnetic forces between balls allowed the system to be more stable with an empty outer shell than at lower currents. We might draw comparisons between the 1-8 and 2-7 configurations and the ground and excited states for atoms.

We identified 4 different configurations for the $N = 9$ system, but only one configuration for the $N = 19$ and 37 systems. In the $N = 9$ system the magnetic force acting on each ball is weakest when holding current constant, so these weaker forces likely allow for different configurations to emerge at varying stability rates. This idea is reinforced by the probability results in table VI. We found that as the current increased the probability of the $N = 9$ system reaching an equilibrium in the 2,7 configuration increased.

We also observed interesting qualitative differences in the organization of the 2,7 configuration. It seems that there are 3 possibilities of how the balls can arrange themselves. The first is the configuration seen in figure (21), which we refer to as the straight pattern because

one of the balls in the inner shell is directly aligned with a ball on the outer shell. The second arrangement is referred to as the skewed pattern because one of the balls in the inner shell is slightly misaligned with a ball on the outer shell. The third has the three central spheres completely misaligned, which was not observed as frequently.

The observed melting behavior can be explained by the magnetic forces between the ferromagnetic balls. As the current decreases, the repulsive magnetic forces between balls also decreases. This allows the balls to transition between shells due to the energy injected into the system by the shaker. We noticed that the threshold current for melting for 37 balls was higher than for 19 balls. This is an unexpected result because the magnetic force on an individual ball should be larger at the same current as the number of balls increases.

VII. Experiment 4

In the fourth experiment we compare the velocity distribution of various multi-ball systems to the 2-D Maxwell Boltzmann distribution.

A. Methods

1. 2-D Maxwell Boltzman

The speed distribution of particles in 2 dimensions is given by the following equation:

$$P(v) = \frac{mv}{k_B T} \exp\left(\frac{-mv^2}{2k_B T}\right) \quad (19)$$

Equation (19) gives the probability of finding a particle moving with any speed v in the system. In our experiment, we will be fitting the velocity distribution of our N ball systems to the 2-D Maxwell Boltzmann equation, however, we will be replacing $\frac{m}{k_B T}$ with a value referred to as the Pseudo-Temperature. This term will be the fitting parameter for our data and will absorb the term $\frac{m}{k_B T}$. We are only interested in using the Pseudo-Temperature as a metric to fit our data and compare the energy levels of each system of N balls. Since we are not interested in determining the actual temperature of the system, as it is macroscopic, this parameter will suffice. The adjusted equation is:

$$P(v) = \frac{v}{T_p} \exp\left(\frac{-v^2}{2T_p}\right) \quad (20)$$

where T_p is the pseudo-temperature. Assuming that the mass of each ferromagnetic ball is identical, this

substitution should work as expected for our fits and comparisons. We expect that the magnetic interactions between the ferromagnetic balls in the presence of an external AC field will cause the multi-ball system to behave like a gas and obey the 2-D Maxwell Boltzmann Distribution.

2. Equipartition of Energy

The equipartition theorem states that for a system in thermal equilibrium, each degree of freedom will contribute $\frac{1}{2}K_B T$ energy to the system. Defining the total kinetic energy in our 2-D system of N balls as:

$$KE = \frac{1}{2}mv_x^2 + \frac{1}{2}mv_y^2 \quad (21)$$

we can expect the energy in the proper x and y coordinate to be equal. This subsequently means that the distribution of velocities in the x and y coordinate should also be identical if the axes are properly aligned.

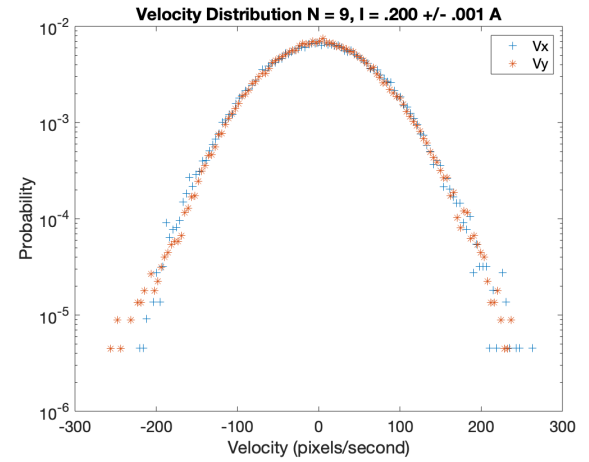


FIG. 31. Example of the velocity distributions between the x and y directions. Created using [14].

3. Rotation Angle

The energy of the multi-ball system is directly proportional to the velocity of each ball. Between a time t_1 and t_2 , each ball in the system will have a velocity in the x direction and a velocity in the y direction if the system is approached using the 2-D analog. The x and y axes of our camera do not necessarily correspond to the x and y axes of the system.

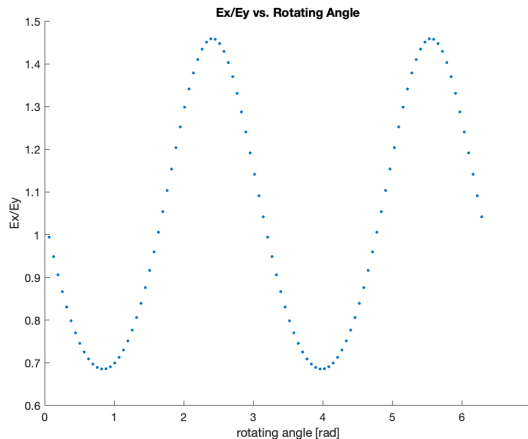


FIG. 32. Example of the energy partition between x and y directions as a function of rotation angle. Created using [14].

Following the equipartition theorem, the energy of the multi-ball system should be evenly distributed between the x and y coordinates. To properly align our axes with the axes of the system, we rotate our axes by an angle θ that results in an even energy distribution between the x and y axes of the 2-D analog. Our axes are rotated using the following rotation matrix [14] :

$$\begin{bmatrix} \cos(\theta) & -\sin(\theta) \\ \sin(\theta) & \cos(\theta) \end{bmatrix}$$

We expect that for a properly rotated system, the distribution of the x and y velocities will have a kurtosis of around 3, which indicates they fit a Gaussian distribution.

4. Equipment

For the final part of the experiment, we kept the set-up similar to that of the third experiment. There are no additions.

5. Procedure

Utilizing N = 9, 19, and 37 ball configurations, we took a video of each system for approximately 6,000 frames. We tracked the resulting videos in ImageJ to obtain coordinate values. Multiple currents were tested for each configuration in order to achieve different velocity distributions. We analyzed the 2D velocity distributions and checked if our results can be fit to the Maxwell Boltzmann Distribution using MATLAB software [14].

B. Results

1. Pseudo-Temperature

We calculated pseudo-temperature values at varying currents for N = 9, 19, and 37 by fitting velocity distribution data to equation (20). Since identical balls were used throughout every trial, we can use the pseudo-temperature values to directly compare the energy across each multi-ball system.

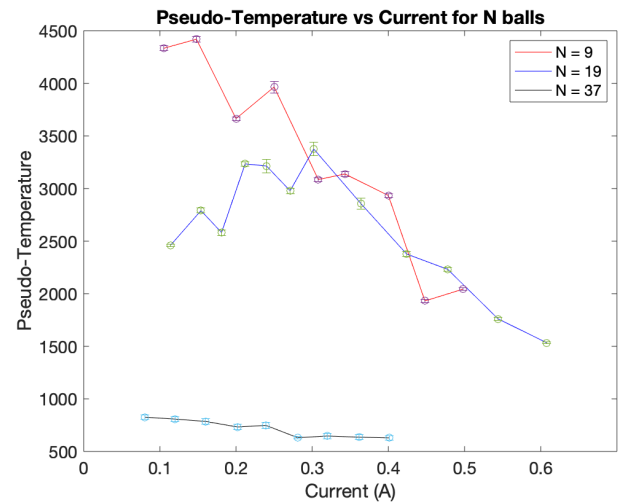


FIG. 33. Pseudo-temperature comparisons between N = 9, 19, and 37 balls. All values are significantly different from 0 ($p < .01$). Created using [14].

Qualitatively, we observed an overall decreasing trend in energy as current increased in the N = 9 ball system. In the N = 19 ball system, we observed an initial increasing trend as current rose to around .3 A, followed by a decreasing trend as current continued to increase. For N = 37 balls, the energy follows a fairly constant trend as current increases.

We also notice that at currents around .1 A, the Pseudo Temperature values across the three systems are significantly different. The values for the N = 37 system are significantly smaller than any of the values for the other two systems, with the pseudo-temperature of the N = 9 system being the largest ($p < .01$).

2. Rotation Angle and Kurtosis

TABLE VII. Equipartition rotation angles and average kurtosis of x and y velocities against current for N = 9.

Current (A)	Rotation Angle (rad)	Average Kurtosis
.498 (.001)	1.06 (.01)	2.771 (.001)
0.448 (.001)	1.08 (.01)	2.693 (.001)
0.400 (.001)	1.01 (.01)	2.939 (.001)
0.343 (.001)	0.44 (.01)	3.002 (.001)
0.308 (.001)	0.98 (.01)	2.957 (.001)
0.250 (.001)	0.49 (.01)	3.001 (.001)
0.200 (.001)	0.26 (.01)	3.038 (.001)
0.148 (.001)	1.00 (.01)	2.829 (.001)
0.105 (.001)	0.53 (.01)	2.994 (.001)

We can observe a general convergence of the kurtosis for the N = 9 system to a value of 3 as the current decreases, with an outlier for a current of .148 (.001) A. The rotation angle necessary for equipartition does not appear to follow a significant trend.

TABLE VIII. Equipartition rotation angles and average kurtosis of x and y velocities against current for N = 19.

Current (A)	Rotation Angle (rad)	Average Kurtosis
0.608 (.001)	0.42 (.01)	3.079 (.001)
0.544 (.001)	0.96 (.01)	3.078 (.001)
0.478 (.001)	1.03 (.01)	3.079 (.001)
0.424 (.001)	1.02 (.01)	3.113 (.001)
0.364 (.001)	0.90 (.01)	3.118 (.001)
0.302 (.001)	1.02 (.01)	3.116 (.001)
0.271 (.001)	0.90 (.01)	3.059 (.001)
0.240 (.001)	0.86 (.01)	3.167 (.001)
0.212 (.001)	0.94 (.01)	3.039 (.001)
0.181 (.001)	0.92 (.01)	3.189 (.001)
0.154 (.001)	0.99 (.01)	3.105 (.001)
0.114 (.001)	0.92 (.01)	3.096 (.001)

The rotation angle appears to exhibit a somewhat constant trend, with a significant outlier at a current of .608 (.001) A. The kurtosis values do not seem to follow a significant trend, but are all greater than 3 as opposed to the average kurtosis values for the N = 9 system. We also do not observe the drop off in rotation angle that we did for the N = 9 system.

TABLE IX. Equipartition rotation angles and average kurtosis of x and y velocities against current for N = 37.

Current (A)	Rotation Angle (rad)	Average Kurtosis
0.08048 (.00001)	.61 (.01)	3.169 (.001)
0.12016 (.00001)	.63 (.01)	3.231 (.001)
0.15982 (.00001)	.64 (.01)	3.287 (.001)
0.20189 (.00001)	.60 (.01)	3.285 (.001)
0.23928 (.00001)	.60 (.01)	3.307 (.001)
0.28109 (.00001)	.61 (.01)	3.343 (.001)
0.31970 (.00001)	.61 (.01)	3.342 (.001)
0.36139 (.00001)	.70 (.01)	3.258 (.001)
0.40120 (.00001)	.78 (.01)	3.230 (.001)

The rotation angle appears to maintain a rather constant trend as the current changes, similar to the N = 9 system. The average kurtosis also appears to maintain a somewhat constant trend and all values are significantly greater than the kurtosis values observed in the N = 9 or N = 19 systems.

C. Maxwell Boltzmann

We fit our data for each current across the three N ball systems as shown in tables VII ,VIII, and IX, to the modified 2-D Maxwell Boltzmann distribution given by equation (20). We used χ^2 and the associated p value to evaluate the goodness of fit for each of our data sets. Despite clear differences between fits, the p values were reported as 1 for all currents across each system. This method was not sensitive enough to differentiate between fits that appeared much better than others. Instead, we highlight a strong fit from each N ball system to showcase their behavior and draw general comparisons between current and number of balls.

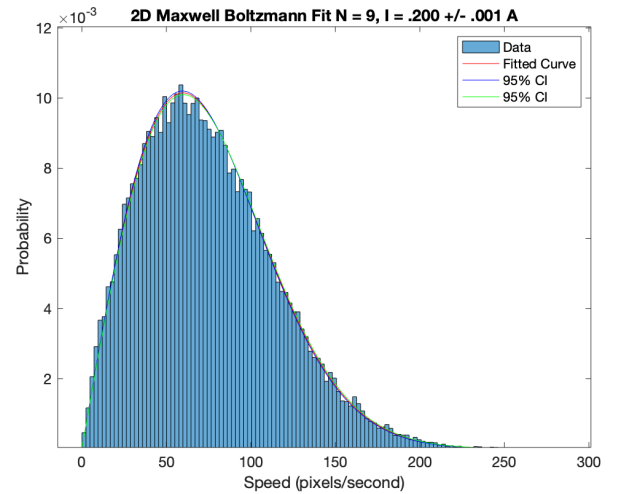


FIG. 34. 2-D Maxwell Boltzmann distribution from equation (20) fit to velocity distribution data for N = 9. $\chi^2(119) = .0013$, p = 1. Created using [14].

The $N = 9$ system exhibited behavior that strongly fits the 2-D Maxwell Boltzmann Distribution at a current of .212 (.001) A.

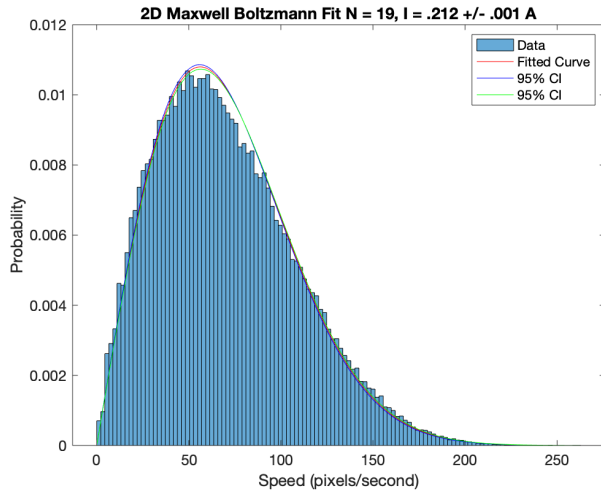


FIG. 35. 2-D Maxwell Boltzmann distribution from equation (20) fit to velocity distribution data for $N = 19$. $\chi^2(119) = .0016$, $p = 1$. Created using [14].

The $N = 19$ system exhibited behavior that strongly fits the 2-D Maxwell Boltzmann Distribution at a current of .200 (.001) A.

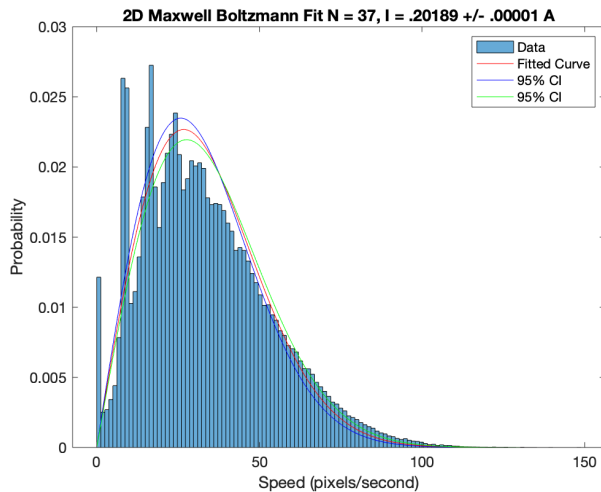


FIG. 36. 2-D Maxwell Boltzmann distribution from equation (20) fit to velocity distribution data for $N = 37$. $\chi^2(119) = .1278$, $p = 1$. Created using [14].

For the $N = 37$ systems, we found that the balls moved too slowly to fit the distribution well. We observe that the distribution fits speeds larger than roughly 60 pixels/second well, but is a poor fit for speeds lower than that. The velocity distribution for $N = 37$ is skewed left and the 2-D Maxwell Boltzmann fit is worse at low speeds than for the $N = 9$ and $N = 19$ systems.

D. Discussion

We found that the pseudo-temperature values across each system were significantly different at a low current. We also found that for all currents, the pseudo-temperature in the $N = 37$ system was significantly lower than for the other two systems. This might be explained by considering the induced magnetic field in each ball as a result of the external magnetic field generated by the current in the solenoid. Regardless of the number of balls in the system, each ball will experience the same magnetic field and thus receive an identical induced field as all of the other balls. As N increases, the strength of the total force exerted on each ball increases, reducing the wiggle-room that each ball has to move within equilibrium. In the $N = 37$ systems, the balls are able to move much less than in the $N = 9$ and $N = 19$ systems, even at low currents.

We found different trends in the average kurtosis and rotation angle values for each system. It is not clear what factors influence these values and further investigation is needed to quantify any meaningful relationships.

We found that $N = 9$ and $N = 19$ systems exhibit behavior that is fit well by the 2-D Maxwell Boltzmann distribution. We observed that this behavior was extremely similar to the distribution around a current of .2 A in both systems. Perhaps this current provides a level of magnetization in the ferromagnetic balls that allows them to act like a gas for specific values of N balls.

The fits for the $N = 37$ system were poor for low speeds. It is likely that the magnetic forces between the balls is too strong at $N = 37$ and the system behaves too much like a solid than a gas or liquid. This is supported by the significantly lower Pseudo-Temperature values for the $N = 37$ systems at all currents, compared to the other two systems.

VIII. General Discussion

The goal of these experiments throughout the semester was to develop an understanding of the possible experiments and methodology used in granular physics.

In experiment 1 we used the gravito-magnetic trap without current to determine an experimental value for the acceleration due to gravity. We achieved an excellent fit of our data to the equation of motion for a damped harmonic oscillator as well as a precise value for g .

In experiment 2 we introduced AC and DC magnetic fields into the gravito-magnetic trap by running varying currents through the surrounding solenoid. We determined experimental relationships between damping

coefficients and the natural angular frequency for both an AC and DC current. We also achieved excellent fits between our data and the theoretical equations for harmonic motion in an AC field, while determining new experimental relationships for the motion in a DC field.

In experiment 3 we used the all-magnetic trap to observe the lattice formation and melting behavior of systems of $N = 9$, 19 , and 37 balls. We found a total of four different lattice formations for the $N = 9$ system, but only 2 distinguishable formations for the $N = 19$ and $N = 37$ systems. We also determined general threshold AC currents at which intra-shell melting can be observed for each system.

In experiment 4 we used the all-magnetic trap to compare the behavior of our three multi-ball systems to the speed distribution given by the 2-D Maxwell Boltzmann distribution. We found a significant decrease in pseudo-temperature values for the $N = 37$ system, and were unable to determine meaningful relationships for either equipartition rotation angles or average kurtosis values. We also found that around a current of $.2$ A, the $N = 9$ and $N = 19$ systems behave very similarly to behavior predicted by a 2-D Maxwell Boltzmann distribution. For the $N = 37$ system, we found that the distribution fits poorly for low speeds at all currents.

Overall, these experiments were successful despite numerous technical and logistical setbacks throughout the semester. They gave us invaluable experience working with granular physics and taught us to incorporate kinematics, electricity, magnetism, thermodynamics, and quantum mechanics together to perform experiments that can be built upon to push the boundaries of physics literature.

IX. Future DirectionssuperscriptBC,BL

There are several next steps that we would like to take with these experiments and our equipment. It would be interesting to observe how the ferromagnetic balls behave as N increases beyond 37 . Throughout the semester we discussed the possibility of analyzing an $N = 61$ system; possibly conducting an experiment to perform an in-depth analyses of how well the velocity distribution fits the 2-D Maxwell Boltzmann as a function of N would provide useful insight. This experiment only featured 3 values of N and thus does not allow us to determine a significant relationship.

In experiments 3 and 4 we utilized a shaker to inject energy into the system. For each trial the frequency of the shaker was held constant throughout both experiments. We might gain more insight into how granular systems, such as our multi-ball systems, behave by comparing their behavior over a range of

shaker frequencies as well as amplitudes.

Does the size of the ferromagnetic balls have an effect on their microscopic behavior? Throughout the semester we discussed the possibility of using larger steel balls and observing their motion. It would be interesting to see if there is an upper limit to the macroscopic particle mass that allows us to observe microscopic behavior.

X. Acknowledgements

We thank Professor Peter Koch (Stony Brook University) for introducing us to Granular Physics and being an excellent mentor throughout this past semester. We also extend thanks to former Stony Brook students Filipe Rudrigues and Yan Ke for providing excellent manuals and software that helped us to complete our experiments. We also thank Professor Dean Schamberger and the rest of the Physics Department for giving us the support needed to complete these experiments despite our lack of laboratory access for the last several weeks of the semester. We finally thank Stony Brook University for providing us with the resources to pursue our education in physics over the last four years.

XI. References

- [1] Mayer, A. M. (1878). Experiments with Floating and Suspended Magnets, Illustrating the Action of Atomic Forces, the Molecular Structure of Matter, Allotropy, Isomerism, and the Kinetic Theory of Gases. *Scientific American*, 5(129supp), 2045-2047. doi:10.1038/scientificamerican06221878-2045supp
- [2] Grzybowski, B. A., Stone, H. A., &; Whitesides, G. M. (2000). Dynamic self-assembly of magnetized, millimetre-sized objects rotating at a liquid-air interface. *Nature*, 405(6790), 1033-1036. doi:10.1038/35016528
- [3] Filinov, A. V., Bonitz, M., &; Lozovik, Y. E. (2001). Wigner Crystallization in Mesoscopic 2D Electron Systems. *Physical Review Letters*, 86(17), 3851-3854. doi:10.1103/physrevlett.86.3851
- [4] Jean, M. S., Even, C., &; Guthmann, C. (2001). Macroscopic 2D Wigner islands. *Europhysics Letters (EPL)*, 55(1), 45-51. doi:10.1209/epl/i2001-00379-x
- [5] Mohazzabi, P., &; Shankar, S. P. (2018). Maxwell-Boltzmann Distribution in Solids. *Journal of Applied Mathematics and Physics*, 06(03), 602-612. doi:10.4236/jamp.2018.63052
- [6] Blundell, S., &; Blundell, K. M. (2006). Concepts in thermal physics. Oxford: Oxford University Press.
- [7] MATLAB. (2019). version 9.7.0.1216025 (R2019b). Natick, Massachusetts: The MathWorks Inc.
- [8] The Maxwell-Boltzmann Distribution (n.d.). Retrieved from <http://alan.ece.gatech.edu/ECE6451/Lectures/StudentLectures/Hill.5p4.MaxwellBoltzmannDistribution.pdf>. Georgia Institute of Technology.
- [9] Rudrigues, Filipe. (n.d.). Static Configurations and Dynamics of Trapped Spheres. Stony Brook University. Unpublished.
- [10] Griffiths, D. J. (1999). Introduction to electrodynamics. Upper Saddle River, NJ: Prentice Hall.
- [11] MATLAB and Image Processing Toolbox Release 2019b, The MathWorks, Inc., Natick, Massachusetts, United States.

- [12] I. F. Sbalzarini & P. Koumoutsakos. (2005). Feature point tracking and trajectory analysis for video imaging in cell biology. *J. Struct. Biol.*, 151(2): 182–195
- [13] Imfindcircles. (n.d.). Retrieved May 7, 2020, from <https://www.mathworks.com/help/images/ref/imfindcircles.html>
- [14] Ke, Yan. (n.d.). Trapped Sphere Analysis Software. MATLAB. Stony Brook University.
- [15] Rudrigues, Filipe. (n.d.). Equipment and Programs. Stony Brook University. Unpublished.
- [16] Keith Brady (2020). CSV with column headers (<https://www.mathworks.com/matlabcentral/fileexchange/29933-csv-with-column-headers>), MATLAB Central File Exchange. Retrieved May 14, 2020.
- [17] Tim Holy (2020). Generate maximally perceptually-distinct colors (<https://www.mathworks.com/matlabcentral/fileexchange/29702-generate-maximally-perceptually-distinct-colors>), MATLAB Central File Exchange. Retrieved May 14, 2020.
- [18] Schneider, C. A.; Rasband, W. S. & Eliceiri, K. W. (2012), "NIH Image to ImageJ: 25 years of image analysis", *Nature methods* 9(7): 671-675, PMID 22930834

A. Data and Software

The originally collected data and related materials are available at the following link: <https://tinyurl.com/ChaseLee445>. The originally written software programs that we used to complete these experiments can also be found in the same directory.

Software and related materials provided by Stony Brook University for the purposes of completing these experiments can be provided upon request.

If there are any additional concerns or questions about the data or software used in these experiments please contact benjamin.chase@stonybrook.edu